

# Surface-Roughness-Scattering in Non-Planar Channels – the Role of Band Anisotropy

Z. Stanojević and H. Kosina

TU Wien, Institute for Microelectronics, Gußhausstraße 27-29/E360, 1040 Wien, Austria

Tel. +43-1-58801-36016, FAX: +43-1-58801-36099, {stanojevic|kosina}@iue.tuwien.ac.at

## I. INTRODUCTION

Non-planar transistor channels used in tri-gate [1] or gate-all-around (GAA) [2] device architectures offer superior electrostatic control, which reduces short-channel effects. The limiting factor in these devices is surface-roughness scattering (SRS) as it is more pronounced in these devices than in planar technologies, which has two reasons: one is that there are more surfaces to scatter off and the other is that sidewall roughness or line-edge-roughness (LER) are harder to control in the fabrication process.

Being of such importance it is surprising to find that a thorough perturbative treatment of SRS is missing in literature. Most low-field mobility calculations for non-planar channels employ phenomenological descriptions or extensions of SRS models for planar structures. Commonly, tri-gate channels are modeled as three separate non-interacting planar channels at the top and each sidewall, and the scattering rate in GAA channels is assumed to be proportional to  $d^6$ , with  $d$  being the diameter. The latter is based on an analysis of quantum wells in Ref. [3].

The only work known to us that rigorously treats SRS for a one-dimensional electron gas (1DEG) is Ref. [4]. The authors calculate the electron mobilities of gated silicon nanowires taking into account both axial and angular interaction of electrons with the rough nanowire surface. The calculations, however, rely on cylindrical symmetry of both real and k-space; this means that first, the model cannot be extended to non-cylindrical geometries, and second, that band anisotropy is completely neglected. The authors approximate the effective masses of  $\langle 100 \rangle$ -oriented nanowires as isotropic in the cross-section, which is questionable in itself and fails to capture the effect of channel orientation. Channel orientation is likely to play an important role in SRS as experimental data from [5] indicates.

This raises the following issues and questions:

- Rotational symmetry even of cylindrical GAA channels is not likely to be valid and must be dropped.
- The  $d^6$ -approximation is only valid in very narrow channels with very low electric fields in the cross-section.
- How to define a “diameter” for a tri-gate device, especially in the presence of electrostatic confinement?
- How can SRS theory for planar and cylindrical geometries be extended to more general surfaces, that don’t even need to be closed shapes?

In this work, we investigate the effect of band structure anisotropy and channel orientation on SRS in non-planar channels such as tri-gate and GAA structures. A new formalism is introduced for calculating SRS rates for non-planar structures.

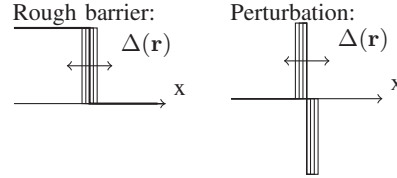


Fig. 1. Abrupt potential step of height  $\Delta V$  in the band edge profile; resulting perturbation with respect to the ideal surface

The formalism is an extension of the theory by Prange and Nee [6] for planar structures, which has been widely used for calculating the conductivity of inversion layers and thin films [7]. We derive matrix elements for open and closed surfaces of arbitrary shape taking anisotropy of the band structure fully into account. Numerical experiments performed on tri-gate and GAA cross-sections indicate that SRS is greatly influenced by band anisotropy and channel orientation.

## II. THEORY

We start by writing the ensemble average of the surface-roughness-induced transition rate for a one-dimensional carrier gas as

$$\langle S_{n,n'}(k,k') \rangle = \frac{2\pi}{\hbar} \langle |H_{n,n';k,k'}|^2 \rangle \delta(E(k) - E(k')), \quad (1)$$

from state  $n$  to  $n'$  and from one-dimensional k-vector  $k$  to  $k'$ . To evaluate the matrix element  $H_{n,n';k,k'}$ , we take a look at the perturbing potential in Fig. 1. The position of an abrupt potential step of height  $\Delta V$  fluctuates as described by the function  $\Delta(\mathbf{r})$ . The resulting perturbing potential is a narrow barrier or well – depending in the sign of  $\Delta(\mathbf{r})$  – of height  $\Delta V$  and width  $\Delta(\mathbf{r})$ . We approximate the perturbing potential by a weighted surface-delta-distribution  $\Delta V \Delta(\mathbf{r}) \delta(\mathbf{r} \in \mathcal{S})$ , where  $\mathcal{S}$  represents the points of the ideal surface. This allows us to convert the evaluation the matrix element  $H_{n,n';k,k'}$  from a volume integration to a surface integration,

$$H_{n,n';k,k'} = \Delta V \int_{\mathcal{S}} \psi_{n,k}^*(\mathbf{r}) \psi_{n',k'}(\mathbf{r}) \Delta(\mathbf{r}) \, dA. \quad (2)$$

The matrix element (2) cannot be evaluated directly since  $\Delta(\mathbf{r})$  is a random function. Instead,  $\Delta(\mathbf{r})$  is characterized by its autocorrelation function  $c(\mathbf{r}) = \langle \Delta(\mathbf{r}') \Delta(\mathbf{r}'+\mathbf{r}) \rangle$  and its 2D Fourier transform  $C(\mathbf{q})$ , i.e. the roughness “power spectrum”. We make no assumptions about the nature of  $c(\mathbf{r})$  or  $C(\mathbf{q})$  in this work, but an exponential autocorrelation function  $c(r) = \Delta_{\text{rms}}^2 e^{-\sqrt{2}r/\Lambda}$  is considered to represent the properties of a rough surface/interface [8] correctly. In the frame of reference of a propagating electron, surface roughness appears as an ensemble of surface-bound phonons with zero frequency and a momentum distribution according to  $C(\mathbf{q})$ .



Fig. 2. Sketch of a tri-gate channel's rough surface denoted by  $\mathcal{S}$ ; electron states ( $\psi_n$  and  $\psi_{n'}$ ) are confined in two dimensions within the fin and interact along the curve  $\mathcal{C}$  (dashed) formed by intersection of  $\mathcal{C}$  with the cross-section plane.

The ensemble average of the square magnitude of (2) can be evaluated.

$$\langle |H_{n,n';k,k'}|^2 \rangle = \iint_{\mathcal{S}} dA dA' \psi_{n,k}(\mathbf{r}) \psi_{n',k'}(\mathbf{r})^* \psi_{n,k}(\mathbf{r}')^* \psi_{n',k'}(\mathbf{r}') \Delta V^2 \langle \Delta(\mathbf{r}) \Delta(\mathbf{r}') \rangle. \quad (3)$$

So far we have made no assumptions about the electron states  $\psi_{n,k}$ . The carriers form a one-dimensional gas and are confined in two spatial dimensions as shown in Fig. 2. We separate the electron states into a two-dimensional standing wave in the cross-section and a plane wave along the channel axis. Using this separation approach, we can rewrite (3) as

$$\langle |H_{n,n';k,k'}|^2 \rangle = \frac{1}{2\pi L^2} \iint_{\mathcal{C}} \iint_0^L f_{n,n';k,k'}(s) f_{n,n';k,k'}^*(s') e^{i(k-k')(z-z')} \langle \Delta(\mathbf{r}) \Delta(\mathbf{r}') \rangle dz dz' ds ds'. \quad (4)$$

The integration across surface  $\mathcal{S}$  was separated into integrations along curve  $\mathcal{C}$ , i.e. the intersection of  $\mathcal{S}$  with the cross-section plane, and a length  $L$  along the channel direction;  $s$  denotes the path coordinate along the curve and  $z$  the axial coordinate. We introduced the form functions  $f_{n,n';k,k'}(s)$  which are defined as

$$f_{n,n';k,k'}(s) = \psi_{n,k}^* \psi_{n',k'} \Delta V. \quad (5)$$

The effect of different effective mass in the channel and the surrounding medium (gate dielectric) can be included in the form functions as

$$f_{n,n';k,k'}(s) = \psi_{n,k}^* \psi_{n',k'} (V_- - V_+) - \nabla \psi_{n,k}^* \cdot \underline{m}_-^{-1} \cdot \nabla \psi_{n',k'} - \nabla \psi_{n,k}^* \cdot \underline{m}_+^{-1} \cdot \nabla \psi_{n',k'}, \quad (6)$$

where the subscripts  $+$  and  $-$  indicate either sides of the interface. In case the cross-section wavefunctions  $\psi_{n,k}$  do not penetrate into the surrounding medium, the expression in (6) can be approximated by

$$f_{n,n';k,k'}(\mathbf{r}) \approx \frac{\hbar^2}{2} m_{\text{barrier}} (\mathbf{n} \cdot \underline{m}_{\text{well}}^{-1} \cdot \nabla \psi_{n,k}^*) (\mathbf{n} \cdot \underline{m}_{\text{well}}^{-1} \cdot \nabla \psi_{n',k'}) \quad (7)$$

Looking back at (4), we recall that  $\langle \Delta(\mathbf{r}) \Delta(\mathbf{r}') \rangle =: c(\mathbf{r})$  and represent the autocorrelation as inverse 2D Fourier transform of the roughness power spectrum,

$$c(\mathbf{r}) = \frac{1}{4\pi^2} \iint_{\mathbb{R}} C(\mathbf{q}) e^{iq_{\perp}(s-s')} e^{iq_{\parallel}(z-z')} dq_{\perp} dq_{\parallel}, \quad (8)$$

separating the roughness “wave vector”  $\mathbf{q}$  into an axial component  $q_{\parallel}$  and a component  $q_{\perp}$  along  $\mathcal{C}$ . Inserting (8) into (4), we arrive at

$$\langle |H_{n,n';k,k'}|^2 \rangle = \frac{1}{4\pi^2 L^2} \iint_{\mathcal{C}} ds ds' \iint_{\mathbb{R}} dq_{\perp} dq_{\parallel} \int_0^L dz dz' f_{n,n';k,k'}(s) f_{n,n';k,k'}^*(s') C(\mathbf{q}) e^{iq_{\perp}(s-s')} e^{i(k-k'+q_{\parallel})(z-z')}. \quad (9)$$

Axial integration of the plane wave term  $e^{i(k-k'+q_{\parallel})(z-z')}$  leads to a  $2\pi L \delta(k-k'+q_{\parallel})$  expression thus simplifying the previous equation to

$$\langle |H_{n,n';k,k'}|^2 \rangle = \frac{1}{2\pi L} \iint_{\mathcal{C}} ds ds' \int_{\mathbb{R}} dq_{\perp} f_{n,n';k,k'}(s) f_{n,n';k,k'}^*(s') C(\mathbf{q}) e^{iq_{\perp}(s-s')}. \quad (10)$$

A change of variables  $s' - s =: s''$  gives

$$\langle |H_{n,n';k,k'}|^2 \rangle = \frac{1}{2\pi L} \int_{\mathbb{R}} C(\mathbf{q}) dq_{\perp} \left[ \int_{\mathcal{C}} \int_{\mathcal{C}} f_{n,n';k,k'}(s) f_{n,n';k,k'}^*(s+s'') ds \right] e^{iq_{\perp}s''} ds'. \quad (11)$$

The term in square brackets represents an autocorrelation of the form functions  $f_{n,n';k,k'}(s)$  and the integration around it is a Fourier transform  $s \mapsto q_{\perp}$ . Using the Wiener-Khinchin theorem we can express the Fourier transform of the autocorrelation of  $f_{n,n';k,k'}(s)$  as square magnitude of its Fourier transform  $F_{n,n';k,k'}(q_{\perp})$  obtaining the final expression for the matrix element and transition rate,

$$\langle |H_{n,n';k,k'}|^2 \rangle = \frac{1}{2\pi L} \int_{\mathbb{R}} |F_{n,n';k,k'}(q_{\perp})|^2 C(\mathbf{q}) dq_{\perp}. \quad (12)$$

$$S_{n,n'}(k, k') = \frac{1}{\hbar L} \int_{\mathbb{R}} |F_{n,n';k,k'}(q_{\perp})|^2 C(\mathbf{q}) dq_{\perp} \delta(E_{n'}(k') - E_n(k)) \quad (13)$$

A few assumptions are contained within this last step of our derivation:

- For closed curves  $\mathcal{C}$  (GAA channel) the Fourier transform is in fact a Fourier series expansion.
- For open curves  $\mathcal{C}$  (tri-gate channel) the wavefunctions are assumed to be square-integrable and so are the form functions  $f_{n,n';k,k'}(s)$ . If the electrons are confined to the fin cross-section electrostatically, the value of  $f_{n,n';k,k'}(s)$  will exponentially decay for  $s \rightarrow \pm\infty$ . This allows to extend the integration over  $\mathcal{C}$  to  $\mathbb{R}$ .
- The roughness power spectrum is isotropic,  $C(\mathbf{q}) = C(q)$ .

### III. COMPUTATION

The wavefunctions  $\psi$  are obtained by solving the closed-boundary Schrödinger equation in 2D in the parabolic band approximation,

$$\frac{\hbar^2}{2} (\nabla \cdot \underline{m}^{-1} \cdot \nabla + V) \psi = E \psi, \quad (14)$$

with anisotropic effective mass tensor  $\underline{m}$ . The equation is discretized on an unstructured triangular mesh using a method

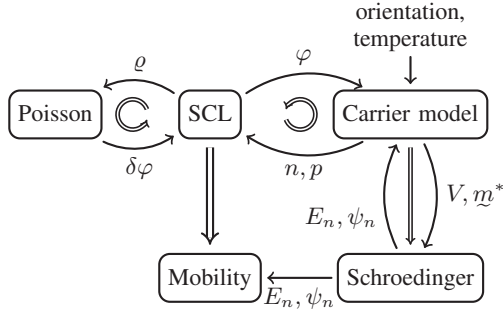


Fig. 3. Overall computational procedure; a self-consistent Schrödinger-Poisson loop (SCL) is run. The subband energies and wavefunctions of the converged solution are used to calculate scattering rates and mobilities. Single arrows represent data flow, double arrows control flow.

reported earlier in [9]. The discretization ensures the correct treatment of anisotropic bands and naturally includes the effect of channel orientation. A self-consistent Schrödinger-Poisson simulation is conducted to obtain the electron concentration in the channel cross-section as well as the wavefunctions for each valley and subband. The computed wavefunctions and energies are used to compute the scattering rates between the subbands which are then used to compute channel conductivities and mobilities using the Kubo-Greenwood formula [10]. Fig. 3 outlines the computational procedure.

Since we are assuming parabolic bands an energy-dependent scattering rate from subband  $n$  to subband  $n'$  can be obtained from (13) and the 1DEG density of states  $g_{1D,n'}(E)$ ,

$$\frac{1}{\tau_{n,n'}(E)} = \frac{1}{2\hbar} \int_{\mathbb{R}} |F_{n,n'}(q_{\perp})|^2 C(\mathbf{q}) dq_{\perp} g_{1D,n'}(E). \quad (15)$$

An efficient procedure was devised to compute the spectral form functions  $F_{n,n'}(q_{\perp})$  required for the integral in (15). The procedure is depicted in Fig. 4. The wavefunctions are used to compute the form functions along the interface curve  $\mathcal{C}$ , which are resampled onto an equidistant  $q_{\perp}$ -grid and fast-Fourier-transformed to obtain their spectral counterparts  $F_{n,n'}(q_{\perp})$ . Having found the spectral form functions  $F_{n,n'}(q_{\perp})$  the scattering rate in (15) is obtained via  $q_{\perp}$ -integration, visualized in Fig. 5. The integral represents momentum conservation in the cross-section plane. In a planar geometry with a two-dimensional electron gas momentum conservation is characterized by a  $\delta(\mathbf{k} - \mathbf{k}' + \mathbf{q})$  term. In a non-planar structure cross-section momentum conservation is not sharply defined and the  $\delta(\mathbf{k} - \mathbf{k}' + \mathbf{q})$  term is replaced by the integral in (15).

In addition to the SRS rate, the electron-phonon scattering rates were also computed. Common literature parameters for phonon scattering in bulk silicon were used with the exception of the acoustic deformation potential, which was set to 14.6 eV due to the proximity of the Si/SiO<sub>2</sub> interface. All rough surfaces were assumed to have exponential autocorrelation with  $\Delta_{\text{rms}} = 0.48$  nm and  $\Lambda = 1.3$  nm [4].

All models were implemented as part of the Vienna Schrödinger-Poisson quantum simulation framework [12].

#### IV. RESULTS

Using our model we investigated the properties of two sets of devices. The first set consists of cylindrical GAA channels of different diameters (3 nm to 14 nm) and orientations ( $\langle 100 \rangle$ ,  $\langle 110 \rangle$ ,  $\langle 111 \rangle$ ). For comparison, the  $\langle 100 \rangle$ -oriented channels

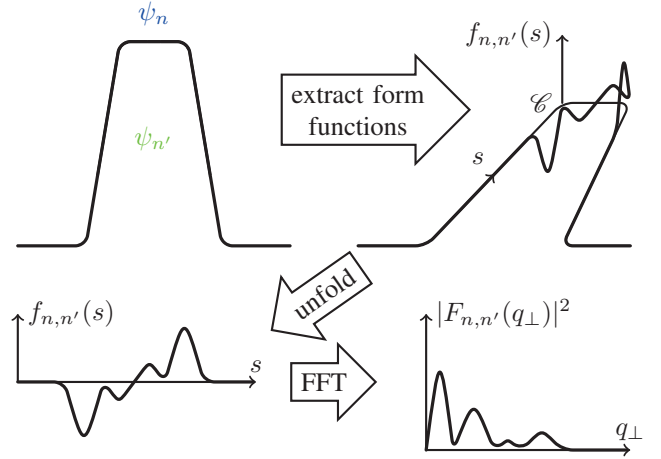


Fig. 4. Computational procedure to obtain the form functions  $f_{n,n'}(s)$  and the spectral form functions  $F_{n,n'}(q_{\perp})$ : For each two cross-section wavefunctions  $\psi_n$  and  $\psi_{n'}$  the expression in (6) is evaluated along the interface curve  $\mathcal{C}$  on the mesh used for computing the states. The form function  $f_{n,n'}(s)$  is interpolated onto an equidistant  $s$ -grid and padded with zeros if  $\mathcal{C}$  is open. The spectral form function  $F_{n,n'}(q_{\perp})$  is computed using the fast Fourier transform (FFT) [11].

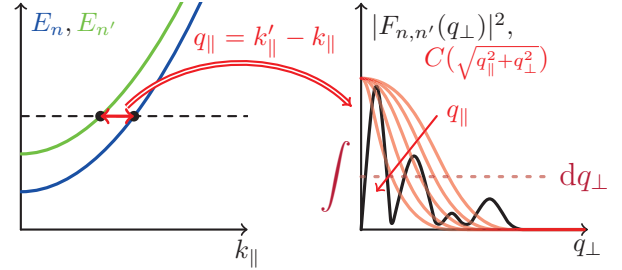


Fig. 5. Calculation of the scattering rate from subband  $n$  to subband  $n'$  from (15); for each energy value the difference of axial  $k$ -vectors is evaluated which represents the axial momentum transfer  $q_{\parallel}$ . The roughness power spectrum  $C(\mathbf{q})$  is offset using  $\sqrt{q_{\parallel}^2 + q_{\perp}^2}$  and its product with the spectral form function  $F_{n,n'}(q_{\perp})$  integrated.

were also simulated with isotropic cross-section mass  $m_{\text{iso}} = 2m_1m_t/(m_1 + m_t)$  [4]. All channels were covered by 1 nm of SiO<sub>2</sub> as well as a metal gate. Fig. 6 shows the self-consistent carrier concentration for the  $\langle 100 \rangle$  and  $\langle 110 \rangle$  channels at 1 V gate bias. Except for ultra-thin channels of 4 nm and below the carrier distribution is clearly anisotropic and one may expect strong deviation from the isotropic approximation also in the channel mobilities. This is in fact the case as seen in Fig. 7. The deviation is especially strong for thicknesses around 5 nm when gate bias is applied. This is the transition region between bulk and layer inversion where a 2D quantum picture of the channel cross-section is necessary.

The second set of devices was constructed to match the cross-section of Intel's 22 nm node tri-gate transistors [1]. Different combinations of channel/substrate orientation ( $\langle 100 \rangle/\langle 010 \rangle$ ,  $\langle 110 \rangle/\langle 001 \rangle$ ,  $\langle 110 \rangle/\langle 1\bar{1}0 \rangle$ ,  $\langle 110 \rangle/\langle 1\bar{1}1 \rangle$ ) were evaluated. Fig. 8 shows the self-consistent electron concentration for the  $\langle 110 \rangle/\langle 001 \rangle$  orientation. The electrons interact with an Si/SiO<sub>2</sub> curved interface comprised of a distribution of surface orientations, which is different for every channel/substrate orientation. This results in heavily orientation-dependent channel conductivity (Fig. 9).

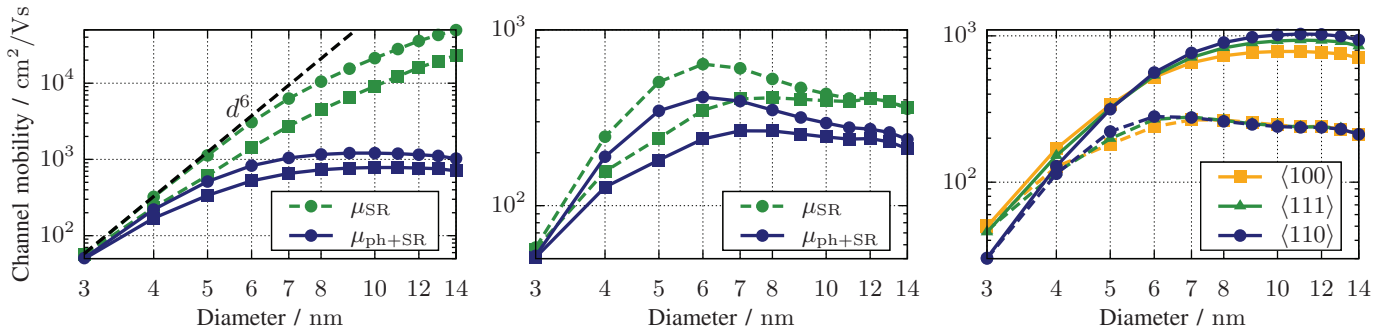


Fig. 7. Thickness-dependent mobilities for cylindrical GAA channels; **left**:  $\langle 100 \rangle$  orientation unbiased; **middle**: 1 V gate bias,  $\blacksquare$  – anisotropic bands,  $\bullet$  – isotropic approximation; the isotropic approximation deviates strongly from the anisotropic results; **right**: comparison of  $\langle 100 \rangle$ ,  $\langle 110 \rangle$ , and  $\langle \bar{1}10 \rangle$  channels; solid lines – unbiased, dashed lines – 1 V gate bias

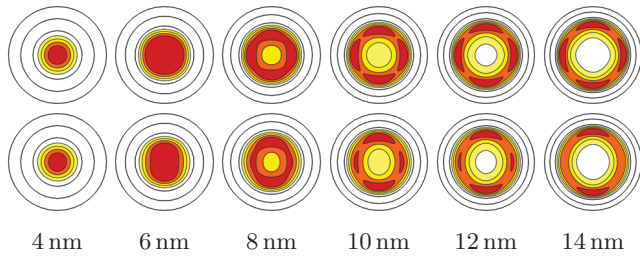


Fig. 6. Self-consistent electron concentration in GAA channels at 1 V gate bias; the top row shows concentrations for  $\langle 100 \rangle$  the bottom row for  $\langle 110 \rangle$  channels. The channel diameter is varied from 4 nm (leftmost) to 14 nm (rightmost) in 2 nm steps. Rotational symmetry is absent in the electron concentration; electrons distribute non-uniformly with respect to azimuthal angle due to band anisotropy.

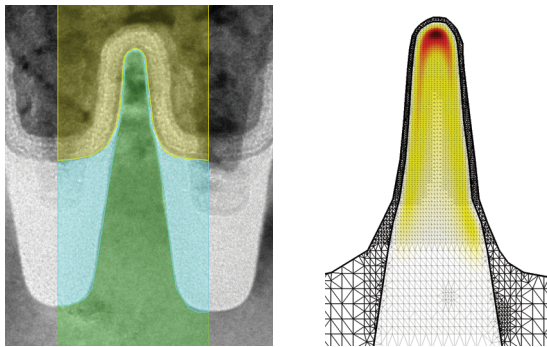


Fig. 8. Left: TEM image of a tri-gate channel cross-section fabricated by Intel [1]; segments of the computational domain are shown in color [13]. Right: Computed self-consistent electron concentration for a  $[110]/(001)$  channel/substrate orientation. The computational grid is visible as well.

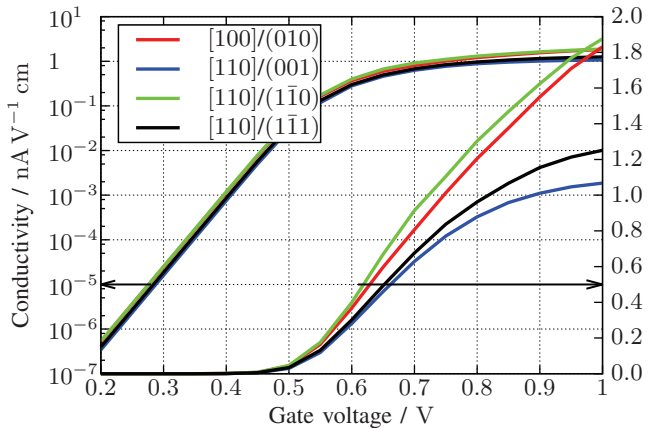


Fig. 9. Channel conductivity vs. gate voltage for the device shown in Fig. 8; Different channel/substrate orientations show different behavior due to orientation-dependence of SRS.

## V. CONCLUSION

We developed a new generic method for evaluating the surface-roughness-induced scattering rate in non-planar semiconductor structures. The method accurately captures band anisotropy and the roughness-induced momentum transfer between the confined states. Strong dependence of SRS-limited electron mobility on crystal orientation was observed with  $\langle 100 \rangle$  and  $[110]/(1\bar{1}0)$  being the optimal orientations.

## ACKNOWLEDGMENT

This work has been supported by the Austrian Science fund through contracts F025 and I841-N16. We acknowledge our partner Global TCAD Solutions LLC.

## REFERENCES

- [1] C. Auth *et al.*, “A 22nm high performance and low-power CMOS technology featuring fully-depleted tri-gate transistors, self-aligned contacts and high density MIM capacitors,” in *VLSIT*, 2012, pp. 131–132.
- [2] S. Bangsaruntip *et al.*, “Gate-all-around silicon nanowire 25-stage CMOS ring oscillators with diameter down to 3 nm,” in *VLSIT*, 2010, pp. 21–22.
- [3] Ken Uchida *et al.*, “Carrier scattering induced by thickness fluctuation of silicon-on-insulator film in ultrathin-body metal-oxide-semiconductor field-effect transistors,” *Applied Physics Letters*, vol. 82, no. 17, pp. 2916–2918, 2003. [Online]. Available: <http://link.aip.org/link/APL/82/2916/1>
- [4] S. Jin *et al.*, “Modeling of electron mobility in gated silicon nanowires at room temperature: Surface roughness scattering, dielectric screening, and band nonparabolicity,” *J. Appl. Phys.*, vol. 102, no. 8, p. 083715, 2007. [Online]. Available: <http://link.aip.org/link/JAP/102/083715/1>
- [5] S. Takagi *et al.*, “On the universality of inversion layer mobility in Si MOSFET’s: Part II-effects of surface orientation,” *IEEE T. Electron. Dev.*, vol. 41, no. 12, pp. 2363–2368, 1994.
- [6] R. E. Prange *et al.*, “Quantum Spectroscopy of the Low-Field Oscillations in the Surface Impedance,” *Phys. Rev.*, vol. 168, pp. 779–786, Apr 1968. [Online]. Available: <http://link.aps.org/doi/10.1103/PhysRev.168.779>
- [7] D. Esseni, “On the modeling of surface roughness limited mobility in SOI MOSFETs and its correlation to the transistor effective field,” *IEEE T. Electron. Dev.*, vol. 51, no. 3, pp. 394–401, march 2004.
- [8] S. M. Goodnick *et al.*, “Surface roughness at the Si(100)-SiO<sub>2</sub> interface,” *Phys. Rev. B*, vol. 32, pp. 8171–8186, Dec 1985. [Online]. Available: <http://link.aps.org/doi/10.1103/PhysRevB.32.8171>
- [9] Z. Stanojevic *et al.*, “A versatile finite volume simulator for the analysis of electronic properties of nanostructures,” in *SISPAD*, sept. 2011, pp. 143–146.
- [10] D. A. Greenwood, “The Boltzmann Equation in the Theory of Electrical Conduction in Metals,” *Proc. Phys. Soc.*, vol. 71, no. 4, p. 585, 1958. [Online]. Available: <http://stacks.iop.org/0370-1328/71/i=4/a=306>
- [11] O. Baumgartner *et al.*, “Efficient simulation of quantum cascade lasers using the Pauli master equation,” in *SISPAD*, sept. 2011, pp. 91–94.
- [12] Z. Stanojevic *et al.*, “VSP - a Quantum Simulator for Engineering Applications,” in *IWCE*, 2013, pp. 93–94.
- [13] “GTS Framework,” [Online; accessed 2013-07-02]. [Online]. Available: <http://www.globaltcad.com/en/products/gts-framework.html>